ALMA MATER STUDIORUM · UNIVERSITÀ DI BOLOGNA

Scuola di Scienze
Dipartimento di Fisica e Astronomia
Corso di Laurea in Fisica

Classification of optical properties in the Adriatic and Black Sea

Relatore:
Prof. Francesco Trotta

Correlatore:
Prof.ssa Nadia Pinardi

Presentata da:
Martina Tolomei

Anno Accademico 2022/2023

Abstract

The propagation of solar radiation into the water column is influenced by various factors. One key factor is the presence of chlorophyll, which absorbs solar radiation at different wavelengths and affects the optical properties of water. This thesis aims to analyze different schemes of solar radiation penetration along the water column to determine the most suitable model for a specific type of water. The study employs sensitivity experiments carried out from 2010 to 2019, focusing on two specific locations of interest: the southern Adriatic and the Black Sea. These findings emphasize the importance of accurately representing solar radiation penetration in numerical models for a better understanding of water characteristics.

Sommario

La propagazione della radiazione solare nella colonna d'acqua è influenzata da diversi fattori. Uno dei più rilevanti è la presenza di clorofilla, che assorbe la radiazione solare a diverse lunghezze d'onda e influenza le proprietà ottiche dell'acqua.

Questa tesi si propone di analizzare diversi schemi di penetrazione della radiazione solare lungo la colonna d'acqua al fine di determinare il modello più adatto per una tipologia specifica. Lo studio si basa su esperimenti di sensitività condotti dal 2010 al 2019, concentrandosi su due specifiche aree di interesse: il sud dell'Adriatico e il Mar Nero.

I risultati ottenuti sottolineano l'importanza di rappresentare accuratamente la penetrazione della radiazione solare nei modelli numerici per una migliore comprensione delle caratteristiche dell'acqua.

Contents

CHAPTER 1

Introduction

Understanding how light interacts with sea water is fundamental in several fields of study as biological primary production, mixed-layer thermodynamics, photochemistry, lidar bathymetry, ocean-color remote sensing, and visual searching for submerged objects.

Radiative transfer theory is the principal method for modeling radiation propagation in the ocean. In order to simulate the upper ocean thermal structures as realistically as possible, an ocean general circulation model (OGCM) requires accurate solar radiation data, used as the surface boundary condition.

The appropriate choice of absorption schemes of solar radiation is also important for ocean modeling in the upper ocean. The absorption of solar radiation is greatly affected by many factors, such as the wavelength of sunlight, the zenith angle and ocean optical properties. Many absorption schemes have attempted to mimic these processes, but the impact of those schemes on the upper ocean thermal structures is not yet fully understood.

This first chapter provide an overview of the definitions and terminology of radiative transfer as used in oceanography. Various ways of quantifying the optical properties of a water body and the light within the water are described. A detailed description of the parameter known as the diffuse attenuation coefficient, $\mathrm{K_d}$, are provide.

Absorption of solar radiation plays a major role in heating the upper ocean layers, it is essential for modeling physical, chemical and biological processes. The Jerlov's classification of water types based on the vertical attenuation in the sea of spectral downward irradiance is then presented. The chapter closes with the objectives of this research study.

1.1 Characteristics of radiative transfer

We start this chapter with the definition of some fundamental quantities used to describe the electromagnetic radiation in radiometric terms. In particular we will define the radiance, the irradiance and the photosynthetically available radiation (PAR). We will adopt the description presented by Apel [1], which focuses on measurable quantities rather than conventional descriptions based on magnetic and electric fields.

1.1.1 Radiance and Irradiance

Radiance, often called "specific intensity", is the fundamental radiometric quantity. It can be defined as the amount of light passing through or emitted from a specific area within a given solid angle.

Radiance is therefore a directional quantity: the radiance of a surface depends on the direction from which it is being observed Fig. 1.1a. Spectral radiance, specifically, refers to the radiance per unit wavelength or frequency and is expressed as:

$$L_\lambda(z,\theta,\phi,t) = \frac{d^4Q}{dt\,dA\,cos\theta\,d\Omega\,d\lambda} \tag{1.1}$$

where Q is the radiant flux of power [J], θ is the angle between the surface normal and the specified direction, Ω is the solid angle [sr], A is the area of the source [m^2]. The SI units of spectral radiance is J/(sr m^2 s nm) (Joule per seconds, per stederadian, per square meter, per nm).

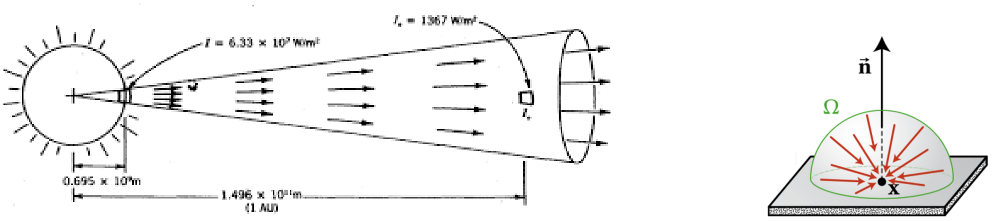

(a) Divergence of energy from the sun to the earth. (b) Scalar irradiance per unit area.

Figure 1.1: Radiance and irradiance.

Radiance is a measurable quantity that serves as a useful concept in optical oceanography to describe the reflection or emission of solar radiation. From spectral radiance, we can derive the concept of spectral irradiance, also called radiant flux density, denoted as I_λ(z,t), which represents the (spectral) radiant flux hat passes through a unit area. The commonly used irradiances are:

- the scalar irradiance: The radiant power per unit area from all directions onto a spherical collecting surface (Fig. 1.1b). It is defined by integrating the radiance over all angles (4π) :
- downward (upward) plane irradiance : The downward (upward) directed radiant power per unit area onto an upward (downward) facing horizontal surface. The downward plane irradiance minus the upward plane irradiance is called the net plane irradiance.

$$I_\lambda(z,t) = \int_{4\pi} L_\lambda(z,\theta,\phi,t)\, d\Omega \tag{1.2}$$

In the SI system, it is specified in units of J/(s m^2 nm) (Watts per square meter). By integrating the spectral scalar irradiance over all wavelengths, we can obtain the total radiation flux at a specific depth z. Different wavelengths of radiation are absorbed at varying levels within the ocean, that's why quantifying the spectral radiance is important. In this way, we can understand the distribution of energy absorption among the various parts of the electromagnetic spectrum.

1.1.2 Photosynthetically Active Radiation (PAR)

According to McCree (1971 [20]), PAR (Photosynthetically Active Radiation) is the wavelength range between 400 and 700 nm that photosynthetic organisms actually utilise for photosynthesis. It controls primary productivity, or the rate of carbon fixation by terrestrial and aquatic plants. Primary productivity varies annually and is influenced by a number of factors, including latitude, the angle of the sun's zenith, and wind stress. The typical range is 0.42 to 0.50, with summertime values being somewhat higher and wintertime values being somewhat lower. PAR is traditionally defined as (e.g., Asrar et al., 1989 [3])

$$PAR(W\,m^{\text{-2}}) = \int_{400}^{700} I(\lambda)\,d\lambda \tag{1.3}$$

Where I(λ) is the downward spectral solar irradiance at wavelength λ.
Since photosystem processes are quantum reactions, McCree [20] suggested that the number of photons (light quanta) is a better indicator of photosynthetic efficiency than energy because photosystem operations are quantum reactions. It is useful to consider the equation:

$$PAR(E\,m^{\text{-2}}\,s^{\text{-1}}) = \frac{1}{h\,c}\int_{400}^{700} \lambda\,I(\lambda)\,d\lambda \tag{1.4}$$

Where h is Plank's constant and c is the speed of light. PAR is now measured in Einsteins per square meter per second.

1.2 Optical properties of the water (IOPs and AOPs)

This section describes the optical characteristics of the aquatic medium that the light travels through as well as the characteristics of the underwater radiation field. The two phenomena of absorption and scattering are now briefly discussed, followed by a discussion of the optical properties, particularly the absorption coefficient, the scattering coefficient, and the beam attenuation coefficient.

According to Kirk (1984 [16]), the inherent optical properties of oceanic water and its main constituents; dissolved yellow substances, particulate organic matter (POM), phytoplankton, and inorganic particles cause solar flux that penetrates through the water column to change significantly in intensity, spectral composition, and angular distribution.

Inherent optical properties (IOPs), or characteristics of a medium that are independent of the ambient light field in the medium, are defined here. The IOPs are various measurements of a water body's absorption and scattering characteristics. The absorption coefficient can be used to calculate all other IOPs, including the scattering and beam attenuation coefficients. The apparent optical properties (AOPs), on the other hand, are the properties of a medium that depend on both the medium (the IOPs) and the geometric (directional) structure of the ambient light field. These characteristics demonstrate enough regular features and stability to be helpful descriptors of the body of water. Different reflectances, average cosines, and diffuse attenuation coefficients are the most often utilized AOPs.

.

1.2.1 Absorption

One of the processes that can happen when the sunlight interacts with the aquatic medium is absorption. Absorption is highly spectrally dependent, instead of scattering which is not. In the visible region of the spectrum, natural water is characterised by a weak absorption in the blue band and strong in the red, and varies with temperature and salinity. This low absorption in the visible spectrum's blue region is precisely what gives the sea its distinctive blue color. The absorption coefficient can be defined as the total of the absorption coefficients for each component:

$$a(\lambda) = \sum_{i=1}^{N} a_i(\lambda) \tag{1.5}$$

Where N is the total number of absorbing components and (i) represents each component. The primary absorbing components include phytoplankton and other substances such as inorganic suspended particles, non-living organic particulate matter, or detritus. Absorption plays a vital role in phytoplankton physiology because light received by phytoplankton supplies the energy that drives photosynthesis. The chlorophyll-a pigment is one of the most important phytoplankton pigments, and its light absorption is related to its characteristics.

Peaks of absorption are found in the blue and red regions of the spectrum. This contribution is significant for most oceanic water containing a high chlorophyll concentration. According to the research carried out by Baker and Lavelle in 1984 [4], the degree of light absorption caused by these materials varies noticeably depending on the position and particle size. The measurement of pure water's absorption coefficients shows significant fluctuations, with the blue portion of the spectrum showing the highest variances. These variations are probably caused by organic matter contamination.

1.2.2 Scattering

Consider light travelling from a region with one index of refraction into a region with a different index of refraction to explain when scattering occurs simply. Photosynthesis is unaffected by light that is elastically scattered by phytoplankton, and the overall amount of scattering is only slightly increased by clean water. Since water scatters light equally in both directions—forward and backward—and the largest particle scattering is accumulated in the forward direction, water is responsible for the majority of the upwelling flux in the ocean. To forecast and comprehend the propagation of light, however, both absorption and scattering are equally essential.

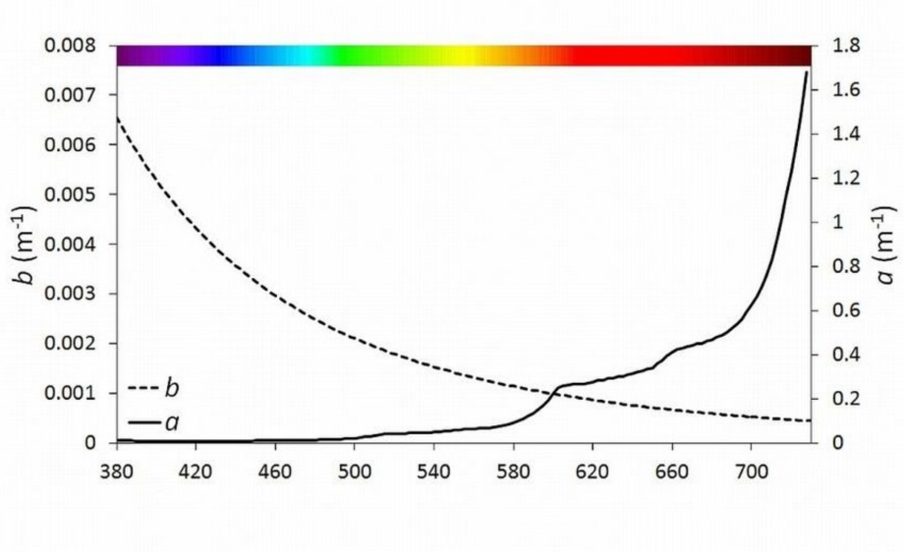

Figure 1.2: The spectral absorption-(a) and scattering-coefficient (b) of pure water measured in the laboratory by respectively Pope and Fry in 1997 [26].

1.3 Diffuse attenuation coefficient $k_d(z)$

Photons are progressively removed from the water column as the solar radiation flux descends through it by absorption, and in addition, it becomes more diffuse as a consequence of scattering (Kirk [17]).
The interaction of radiation with the water and the several dissolved matters causes the light that penetrates the water column to degrade quickly with depth. The intensity of the radiation and the natural optical properties of water dictate the features by which the flux of solar radiation varies with depth. Many parameters must be taken into consideration to define the characteristics of the underwater solar radiation at every depth, but for our purposes, we only need to take into account one of them, irradiance, and two parameters derived from this. As previously stated,

irradiance is defined as the total solar flux incident into a surface per unit area and is expressed in terms of (W m^{-2}). Within an aquatic medium, there is an upward irradiance, $E_u(z)$, and a (often) considerably lower downward irradiance, $E_d(z)$, at any depth z.

The portion of incident radiation that disappears when light descends down the water column is identified as the vertical diffuse attenuation coefficient, or $k_d(z)$. As photons are eliminated by absorption and upward scattering, downward irradiance diminishes with depth in a manner that is approximately exponential. The attenuation coefficient $k_d(z)$ represents this rate of diminution, which is defined as follows for downward irradiance:

$$k_{\mathrm{d}}(z) = -\frac{d\,ln\,E_{\mathrm{d}}(z)}{dz} = -\frac{1}{E_{\mathrm{d}}(z)}\frac{dE_{\mathrm{d}}(z)}{dz} \tag{1.6}$$

Since the angular distribution of the radiation field varies with depth,also $k_d(z)$ changes with depth, but it is easier to practice to assign an average value, k_d, to $k_d(z)$ for the whole illuminated water column.

We can therefore define the variation of downward irradiance with depth in terms of the attenuation coefficient in a simply way:

$$E_{\mathrm{d}}(z) = E_{\mathrm{d}}(0)\; e^{-K_{\mathrm{d}}(z)} \tag{1.7}$$

Where $E_d(0)$ is the downward irradiance at the surface.

K_d varies with wavelength in accordance with the water's absorption spectrum. Since the concentration of optically active dissolved materials might change considerably with depth, it is only reasonable to presume that the coefficient K_d is constant with depth in this formulation.

The optical characteristics of the acquatic medium are formed by the making up of the attenuation coefficient, along with the scattering and absorption coefficients (which are similarly characterized).

The irradiance reflectance, R(z), which is defined as the ratio of the upward to the downward irradiance at any depth, z, is another helpful parameter connected to irradiance.

$$R(z) = \frac{E_{\mathrm{u}}(z)}{E_{\mathrm{d}}(z)} \tag{1.8}$$

In particular, these coefficient are called apparent optical properties (AOPs) because they depend on the distribution of radiation flux, especially near the ocean surface.

1.4 Jerlov water classification

In order to generalize and explain the science of ocean color, natural waters have been classified into optical water types.

In a review paper on water mass classification, Arnone et al.(2004 [9]) credits the Secchi disk (invented around 1865) as the first optical instrument that has been used to measure water transparency.

This rendered it possible to make distinctions between different types of water based on their optical characteristics. Water color classification systems mostly rely on absorption (since scattering contributes to intensity but less so to color). Swedish oceanographer Nils Jerlov suggested categorizing several types of natural waters based on their optical characteristics in 1951 (Jerlov [14]).

The suggestion was based on experimental data collected from various oceanic expeditions, most notably the 1947–1948 Albatross trip. Jerlov measured the amount of solar radiation in the visible spectrum that reached various ocean depths using a photometer with optical filters. The downwelling diffuse attenuation coefficient, $\mathrm{K_d}$, has been determined by comparing the downwelling irradiance at a specific depth to the irradiance recorded at the surface (Williamson and Hollins [32]). Since their initial definition, these Jerlov classifications have undergone modifications.

In his study from 1976, Jerlov [13], presented a classification of ocean water types while taking into consideration the optical properties of the waters in the first 10 meters, which frequently remain homogeneous in the ocean. The location and different concentrations of suspended materials in an ocean determine its optical characteristics. This category separates waters into five types of coastal and open ocean water, ranging in clarity from Jerlov I to Jerlov 9C [12].

The classification is structured as follows: Types I through III are the most transparent, with Type I further subdivided into Groups IA and IB. Instead, types C1 to C9 of coastal waters are the most turbid ones. To characterize the optical features of more turbid coastal waters, the system was expanded by the various types C10-C20 (Piazena and Häder [25] 1997).

Natural waters have been identified as Type I, which has the highest transparency (Smith and Baker [29] 1981). Figure 1.3 summarizes the traits of these 10 different types of water.

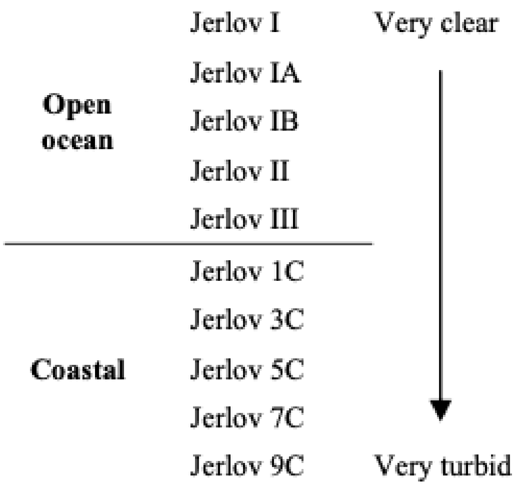

Figure 1.3: Summary of the features of the Jerlov Water types

1.4.1 Relation between K_d and water types

The downwelling diffuse attenuation coefficient, K_d was obtained comparing the downwelling irradiance at a given depth z to the irradiance measured at the surface (z=0).

K_d is known as an apparent optical property (AOP), as it depends on the characteristics of the ocean water and the ambient light from the sun and the sky, as well as the sea state (Preisendorfer [27]). While the standard Jerlov values for K_d can be used in the aforementioned applications, there are other optical parameters that can also be useful to describe different aspects of optical water quality (Williamson and Hollins [32]).

The aim of the classification is that the irradiance attenuation coefficient for any wavelength can be expressed as a linear function of a reference wavelength, usually chosen at 475 nm.

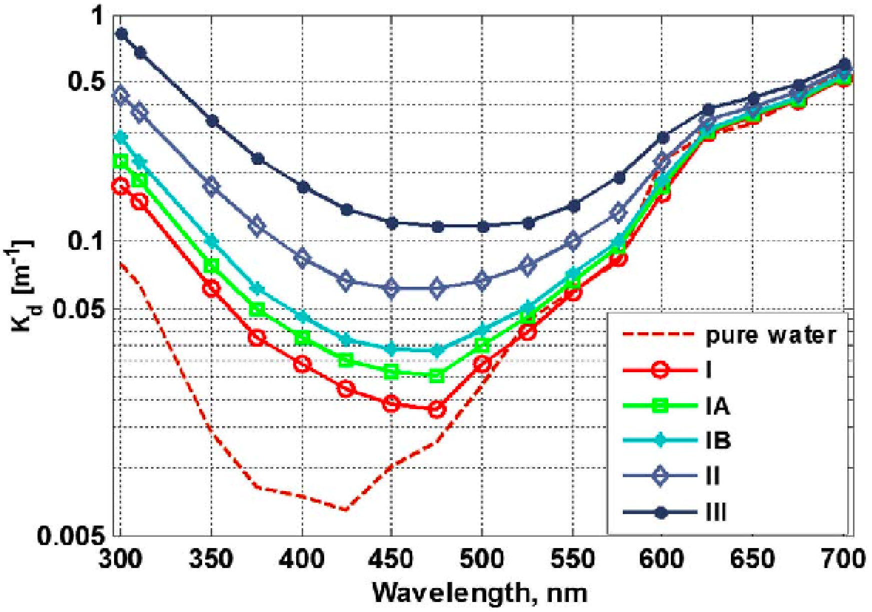

Figure 1.4: Diffuse attenuation coefficients $k_d(z)$ λ of Jerlov oceanic water types I through III, and the absorption spectrum a λ of pure water measured by Solonenko and Mobley [30]

1.5 Thesis Objectives

The objective in this thesis is to investigate the impact of different absorption schemes of solar radiation on the upper ocean thermal structures, at two specific points of interest; one in the southern Adriatic and one in the Black Sea. We used NEMO1D model, a feature included in the NEMO ocean model, to consider only one column of water. NEMO1D is a simple, robust, useful and powerful tool that enables quick and easy investigation of the physical processes affecting the vertical distribution of the ocean state variables.

The initial state of the water columns and the atmospheric variables for the surface boundary condition have been extracted, respectively, by Copernicus Marine Environment Monitoring Service (CMEMS) reanalysis datasets and the European Centre for Medium-Range Weather Forecasts (ECMWF) ERA5 reanalysis datasets. Subsequently, we were able to optically classify various types of water based on the average chlorophyll concentration present.

Sensitivity experiments were then performed from February 1, 2010, to December 31, 2019, at both points of interest. In this way, we deduced how the model reacted to the variation of different penetration schemes and in particular show the impact of those schemes on the upper ocean thermal structures. Regarding the structure of the thesis, the first chapter introduces the theory related to solar radiation along the water column and its optical characteristics. The second chapter describes the model used, the dataset from which the input data are derived, the area of interest, and the different penetration schemes. In the third chapter, a data analysis is performed, comparing the input reanalysis model with the results obtained from our model, highlighting the major differences. Finally, in the fourth chapter, we present the conclusions derived from the analysis of our experiments.

CHAPTER 2

Methods and data

2.1 The NEMO model

In this work, simulations were produced using the 1-D vertical model called NEMO1D, a feature included in the NEMO (Nucleus for European Modeling of the Ocean model [10]) ocean model, to consider only one column of water. The ocean engine of NEMO is a primitive equation model adapted to regional and global ocean circulation problems. It is intended to be a flexible tool for studying the ocean and its interactions with the others components of the earth climate system (atmosphere, sea-ice, biogeochemical tracers, ...) over a wide range of space and time scales.
The Nucleus for European Modelling of the Ocean (NEMO) is a framework of ocean related engines, namely OPA (Océan PArallélisé) for the ocean dynamics and thermodynamics, LIM (Louvain laneuve Ice Model) for the sea-ice dynamics and thermodynamics, TOP (Tracer in the Ocean Paradigm) for the biogeochemistry both transport (TRP) and sources minus sinks (LOBSTER, PISCES).
For a more detailed description of the technical and theoretical details of each model, the reader can refer to Madec [10].
In the next section, we will briefly discuss the main equations of motions and the vertical physics of the 1D NEMO configuration.

2.1.1 Nemo equations of motions

NEMO includes the three-dimensional primitive equations that govern the balance of momentum and physical tracers. These equations are derived through Reynolds averaging of the Navier-Stokes equations and the transport equations for temperature and salinity (Reffray, Bourdalle-Badie, and Calone [28]).
To begin, we can express the three dimensional primitive equations solved by NEMO code and then establish specific equations for the NEMO one-dimensional version. The primitive equations saved by NEMO are based on the Boussinesq and hydrostatic approximations and can be expressed, in a rotating frame of reference, by the following nonlinear partial differential equations:

$$\begin{aligned}\frac{\partial u_i}{\partial t} + u_j \frac{\partial\left(u_i\right)}{\partial x_j} &= -\frac{1}{\rho_0}\frac{\partial P}{\partial x_i} \\ &- \frac{\partial}{\partial x_j}\left(\overline{u_j' u_i'} - v_{\mathrm{mol}}\frac{\partial u_i}{\partial x j}\right) + f_i\end{aligned} \tag{2.1}$$

$$\begin{aligned}\frac{\partial T}{\partial t} + u_j \frac{\partial (T)}{\partial x_j} = -\frac{\partial}{\partial x j}\left(\overline{u_j' T'} - K_{\mathrm{mol}}\frac{\partial T}{\partial x j}\right) \\ + \frac{1}{\rho_0 C_{\mathrm{p}}}\frac{\partial I\left(F_{\mathrm{sol}}, z\right)}{\partial z}\end{aligned} \tag{2.2}$$

$$\begin{aligned}\frac{\partial S}{\partial t} + u_j \frac{\partial (S)}{\partial x_j} = -\frac{\partial}{\partial x j}\left(\overline{u_j' S'} - K_{\mathrm{mol}}\frac{\partial S}{\partial x j}\right) \\ + E_{\mathrm{f}} - P_{\mathrm{f}},\end{aligned} \tag{2.3}$$

where $\mathrm{u}_{\mathrm{i[i=1,2]}}$ represent the mean horizontal components of the velocity along the zonal and meridional directions, $\mathrm{x}_{\mathrm{j[i=1,2,3]}}$ = (x,y,z) are the horizontal and vertical directions, t the temporal dimension, T the temperature, S the salinity, $\mathrm{f}_{\mathrm{i[i=1,2]}}$ the components of the Coriolis term, P the pressure, I the downward irradiance and $\mathrm{F}_{\mathrm{sol}}$ the penetrative part of the surface heat flux, ρ_0 the reference density and C_{p} the specific heat capacity; while $\mathrm{K}_{\mathrm{mol}}$ and $\mathrm{v}_{\mathrm{mol}}$ are the molecular diffusivity and molecular viscosity respectively. Finally, E_{f} and P_{f} express respectively the evaporation and precipitation fluxes; $\overline{u_j' u_i'}$ terms the Reynolds stresses, while $\overline{u_j' T'}$ and $\overline{u_j' S'}$ represent the turbolent scalar flows. Using a first-order approximation, only the vertical component of the average values is maintained.

They are expressed by these coefficients:

$$\overline{u_i'w'} = -v_{\mathrm{t}}\frac{\partial u_i}{\partial z} \tag{2.4}$$

$$\overline{T'w'} = -K_{\mathrm{t}}\frac{\partial T}{\partial z} \tag{2.5}$$

$$\overline{S'w'} = -K_{\mathrm{t}}\frac{\partial S}{\partial z} \tag{2.6}$$

Where v_{t} and $\mathrm{K_t}$ are the vertical turbolent viscosity and diffusivity terms respectively.

The 1D model option in NEMO simulates a stand alone water column. In this configuration, all horizontal gradients are simplified and assumed to be zero. This primitive equation model provides a large variety of applications from short-term forecasts (Mercator Océan and MyOcean/Copernicus) and climate projections (Voldoire et al., 2013 [31]) to process studies (Bernie et al., 2007 [5]). The prognostic variables are the three-dimensional velocity field, the sea surface height (that is non-linear), and two active tracers : the *Conservative Temperature* and the *Absolute Salinity*. The model uses a full or partial step z-coordinate, or s-coordinate , or a mixture of the two in the vertical direction; and for the orizontal direction uses a curvilinear orthogonal grid. The distribution of variables is a three-dimensional Arakawa C-type grid. Therefore, the aforementioned equations (2.1) (2.2) (2.3) reduced to the following:

$$\frac{\partial u_i}{\partial t} = -\frac{\partial}{\partial z}v_{\mathrm{t}}\frac{\partial u_i}{\partial z} + f_i \tag{2.7}$$

$$\frac{\partial T}{\partial t} = \frac{1}{\rho_0 C_{\mathrm{p}}}\frac{\partial I\left(F_{\mathrm{sol}}, z\right)}{\partial z} - \frac{\partial}{\partial z}\,K_{\mathrm{t}}\frac{\partial T}{\partial z} \tag{2.8}$$

$$\frac{\partial S}{\partial t} = -\frac{\partial}{\partial z}\,K_{\mathrm{t}}\frac{\partial S}{\partial z} + E_{\mathrm{f}} - P_{\mathrm{f}}, \tag{2.9}$$

In addition, we have further simplified the terms v_{mol} and $\mathrm{K_{mol}}$ as they are considered negligible compared to the other terms.

Thanks to these simplifications, NEMO demonstrates its suitability as a valuable tool for studying vertical processes within a water column.

2.1.2 Vertical mixing

This section focuses on explaining the vertical turbulent model and draws inspiration from the following research paper (Reffray, Bourdalle-Badie, and Calone [28]).

Vertical mixing plays a vital role in ocean dynamics and requires accurate estimation. Specifically, it gives rise to the mixed layer, a homogeneous layer of the ocean that directly interacts with the atmosphere and can be quantified as the mixed layer depth (MLD). The MLD is of great significance in the exchange of energy between the ocean and the atmosphere and exhibits considerable spatiotemporal variations, including diurnal, seasonal, and synoptic scales. Additionally, variations in MLD have a crucial impact on biogeochemical processes. During winter, episodes of MLD deepening inject nutrients into the euphotic layer, profoundly influencing primary production (Flierl and Davis, 1993 [8]).

Vertical mixing also contributes to convection or seasonal stratification. Lastly, vertical mixing must preserve water masses. In order to specifically study vertical turbulent mixing, we utilize NEMO 1D, a feature integrated into NEMO, which focuses on analyzing a single column of water. NEMO 1D serves as a user-friendly and robust tool that facilitates the examination of physical processes that impact the vertical aspects of ocean state variables, such as turbulence, boundary conditions at the surface and bottom, radiation schemes for penetration, and more. In this thesis, we evaluate the effectiveness of various turbulent schemes available within NEMO, employing a 1-D configuration.

2.1.3 Space and time domain

The 1D option model is designed to simulate processes occurring along a vertical water column. The spatial discretization is based on a three-dimensional field, where specific points of interest can be defined on a grid. The vertical coordinate system divides the water column into a fixed number (N) of vertical levels, with the lowest level representing the seabed.

In the 3D configuration, the main variables can be categorized as scalars (such as temperature, salinity, and density) and vectors (representing the velocity field). The scalar variables are located at the center points of unit cells, while the vector points (u, v, w) are defined at the middle of each face of the cells. This configuration corresponds to the three-dimensional extension of the well-known "C" grid in Arakawa's classification (Mesinger and Arakawa, 1976 [21]).

On the other hand, in the 1D option, all horizontal gradients around the central point are assumed to be zero. In this setup, the central column represents the water, while the surrounding environment is parameterized as the ground and acts as rigid boundaries.

2.2 Implementation of the 1D model

The Nemo 1D model has been implemented in two specific areas. In particular, we selected two points, in South Adriatic and Black Sea, with coordinates :

- 17.70 °N and 41.25 °E for the point in the south Adriatic;
- 30.92 °N and 41.60 °E for the point in the Black Sea;

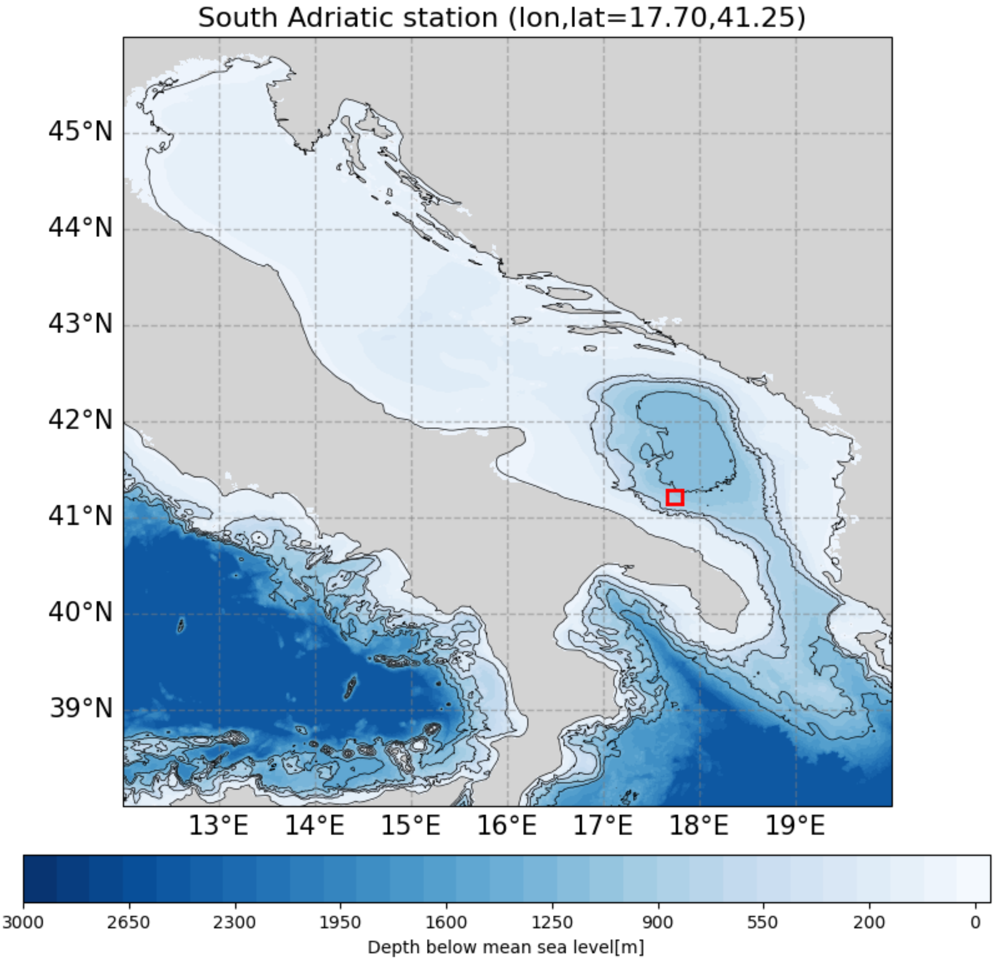

Figure 2.1: South Adriatic: The area enclosed by the red box represents the point of interest. Bathymetric contours are derived from the General Bathymetric Chart of the Oceans GEBCO_2023 dataset.

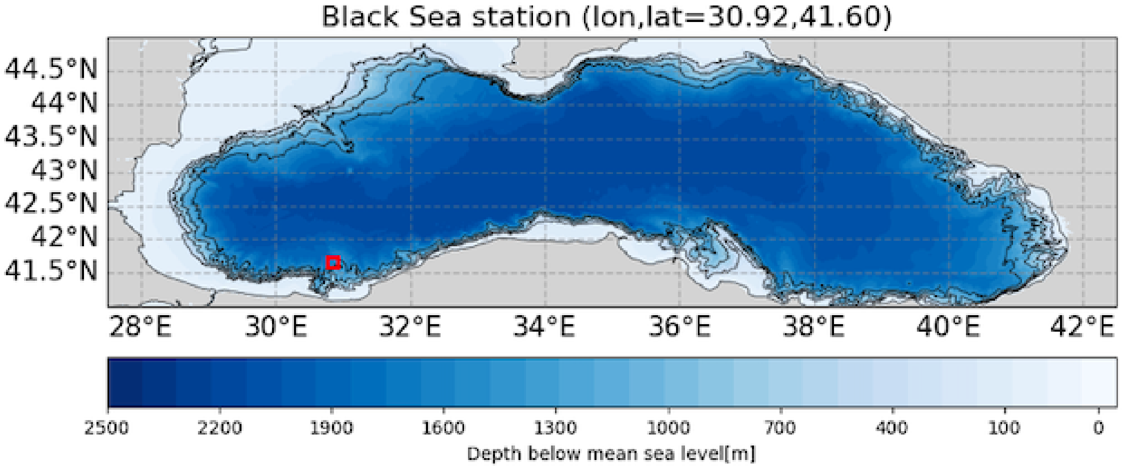

Figure 2.2: Black Sea: The area enclosed by the red box represents the point of interest. Both graphs come from Bathymetry dataset GEBCO_2023.

2.2.1 Adriatic Sea

The Mediterranean Sea's northernmost region includes the Adriatic Sea.
It is bounded on the west by the Italian coast and on the east by the coastlines of Slovenia, Croatia, and Albania. The Adriatic Sea is characterised by a large-scale cyclonic meandering surface circulation, with a northerly flow along the eastern coast and a southerly return flow along the western coast.
Normal speeds are below 10 cm/s, however they can occasionally increase, especially during the wintertime close to the westerly shore (Orlic, Gacic, and Laviolette [23]).
The Otranto Strait acts as the only conduit to the Mediterranean Sea. The Eastern Adriatic Current (EAC), which flows northward along the eastern coast, and the Western Adriatic Current (WAC), that comes southward across the Italian coastline, contribute to the general circulation pattern, that is mostly cyclonic.
According to Fig. 2.3, the EAC reaches the Adriatic through the Otranto Sill on its eastern side and is composed of Modified Levantine Intermediate Water (MLIW) in the bottom layers and Ionian Surface Water (ISW) in the intermediate and surface levels (Artegiani et al. [2]).

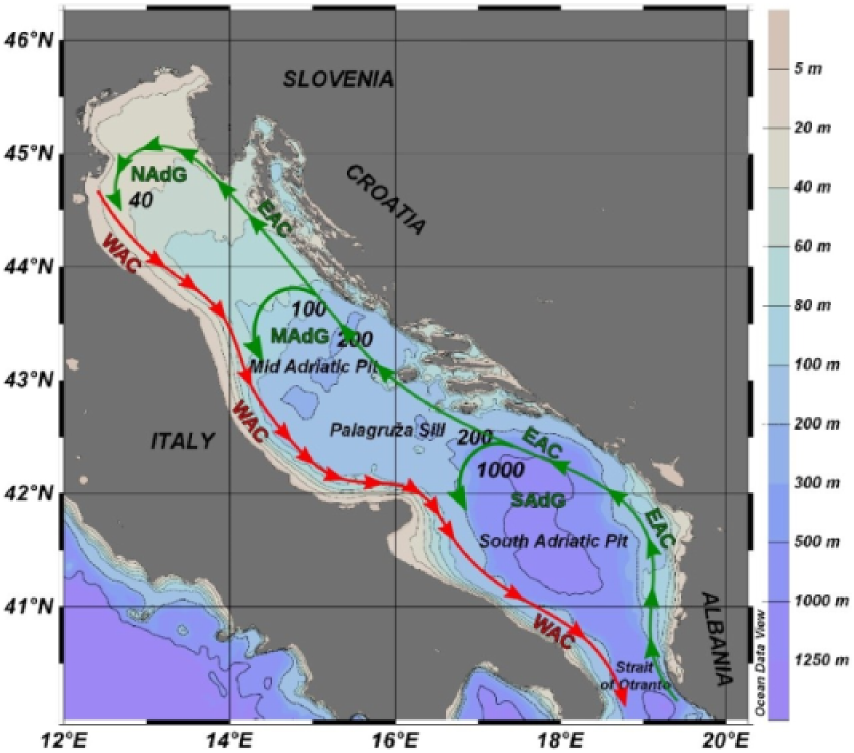

Figure 2.3: Figure shows the bathymetry, morphology, and primary surface circulation of the Adriatic Sea. The photograph was obtained from Artigiani et al ([2]). North Adriatic Gyre, Middle Adriatic Gyre, South Adriatic Gyre, Eastern Adriatic Current, Western Adriatic Current

To the north, the Adriatic sea is featured by low bathymetry (average depth: 35 m) and is greatly influenced by the largest river contributions in the entire basin (Cushman-Roisin et al. [7]). A highly distinct circulation pattern in the surface layers is caused by dominant seasonal winds through the year. Scirocco and Bora are linked to the major wind events over the Adriatic Sea. The former has weak variability and zero gusts since it is a southern-easterly breeze.

The southern Adriatic is distinguished by a well that is 1200 metres deep. In the Otranto Strait, where the Adriatic meets the Ionian Sea, the bottom begins to rise once again. The strait's maximum sill depth is 780 metres, but the mean depth along its 75 km width is 325 metres. To the south, a topographically regulated cyclonic gyre controls the surface circulation over the South Adriatic Pit and appears to partially separate the Middle Adriatic from the effects of the Mediterranean. In addition, it appears that the circulation is influenced by the fresh water coming from the east coast rivers.

The primary cause of coastal upwelling along the straight east coast is off-shore Bora-wind forcing. Even outside of the Adriatic, an intense low-salinity jet along the western shoreline carries water southward while following the coastal contours. The exiting water, (which started in the North Adriatic), flows along the western shelf slope while the MLIW enters along the eastern coast of the intermediate layer. SAW fills the bottom of the South Adriatic Pit.

Under the inflowing MLIW and Ionian surface water, SAW rises from the hole and creates a continuous outflow via the Otranto Strait.

In general, several dense water formations that begin in the northern Adriatic throughout the winter and descend to the Otranto Strait are thought to be the precursors to EMDW, with each region contributing its own characteristics to the forming water mass. The formation of dense water masses throughout the winter and their evacuation from depth are what cause the Adriatic's long-term variability.

.

2.2.2 Blacksea

The Black Sea is a partially enclosed body of water, connected to the Sea of Marmara and the Sea of Azov through narrow straits such as the Bosporus and Kerch Straits. Its drainage area spans across significant parts of Europe and Asia.

Despite evaporation rates exceeding precipitation, the Black Sea maintains a substantial freshwater influx relative to its volume, giving it the characteristics of an estuarine basin.

Due to the considerable freshwater input and the restricted opening at the Bosporus Strait, the exchange between the Black Sea and the Sea of Marmara is asymmetrical. The outflowing surface current transports twice as much water as the inflowing deep counter-current, resulting in the Black Sea's surface salinity being approximately half that of the Mediterranean Sea. Unlike other large estuarine basins, such as the Baltic Sea, the Black Sea stands out as a deep basin with a substantial shelf area, reaching a maximum depth of approximately 2200 meters.

Notably, the presence of cold intermediate water (CIW) mass, characterized by temperatures lower than the average annual temperature of both surface and deep layers, is a direct result of the remarkably stable stratification. This cold intermediate layer (CIL) is formed through winter cooling followed by the dispersion of CIW throughout the sea, typically occupying a depth range of 50 to 100 meters below the surface.

The circulation is purely cyclonic and the presence of haline buoyancy anomalies at the sea surface leads to an intensified cyclonic circulation pattern; primarily driven by the inflow of freshwater along the coastal areas. This circulation pattern typically manifests as two main interconnected gyres systems that encloses the entire basin as shown in Fig. 2.4.

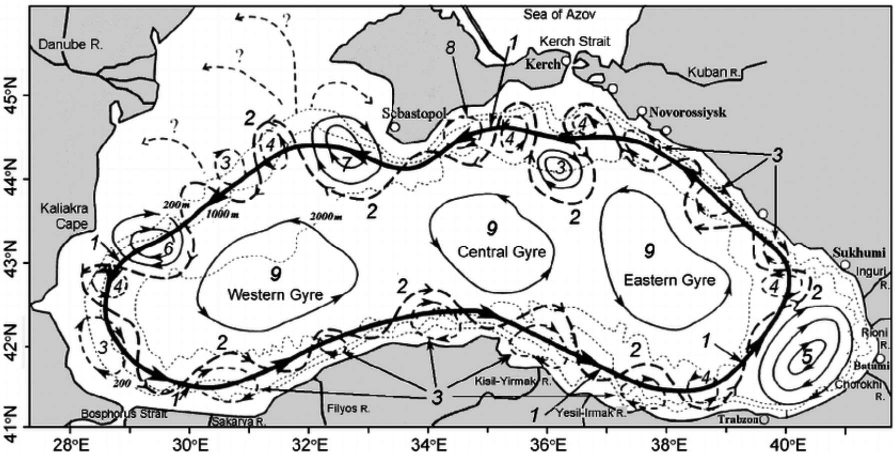

Figure 2.4: Figure shows the schematic of the Black Sea surface circulation. The bold lines indicate recurrent features of the general circulation. The leading gyres are the western and the eastern. The image is obtained from Korotenko ([18])

2.3 Source Datasets

Oceanic initial conditions and atmospheric forcing fields needed to be provided to the NEMO1D model in order to perform our simulations. To capture the necessary inter-annual variability of the marine ecosystem at the selected sites, simulations were executed from 2010 to 2019. The wide range of available datasets for temperature, salinity, and nutrients has made this method possible. The products used for atmospheric forcing and ocean fields will be described in the next section.

2.3.1 Atmospheric forcing and input variables

The products used for the atmospheric forcing are the same for both points of interest. It is provided by the European Centre for Medium-Range Weather Forecasts (ECMWF). This dataset is referred to as: ERA5 reanalysis. ERA5 reanalysis produced within the Copernicus Climate Change Service (C3S) [11]. This reanalysis provide atmospheric variables with a resolution of 1/4°, and a hourly temporal resolution. In the NEMO ocean model it is used to provide the surface boundary conditions. It currently plays a big role in applications for climate monitoring. The monthly C3S climate bulletins for surface air temperature, and hydrological variables are based on ECMWF reanalysis.

The Reanalysis timeseries is available on the Copernicus Marine server [6] and has been available since January 1, 1987. It is extended twice a year (or less frequently, depending on the availability of the reprocessed observational data).

Variable	**Unit**	**Period**	**Frequency**
Wind speed at 10 m	m/s	1980-2018	Hourly
Air temperature at 2 m	°C	1980-2018	Hourly
Dew point temperature at 2 m	°C	1980-2018	Hourly
Specific humidity at 2 m	Kg Kg^{-1}	1980-2018	Hourly
Snowfall and Precipitation	Kg m^{-2} s^{-1}	1980-2018	Hourly
Longwave and Shortwave radiation	W m^{-2}	1980-2018	Hourly

Table 2.1: Summary of the reference units, temporal range, and data frequency.

On the following page, a series of plots (Fig. 2.5) related to the Black Sea are displayed, showing the variations of all atmospheric variables throughout the entire simulation period. Alongside the plots, histograms are provided to highlight the average value of each variable and their measured frequency.

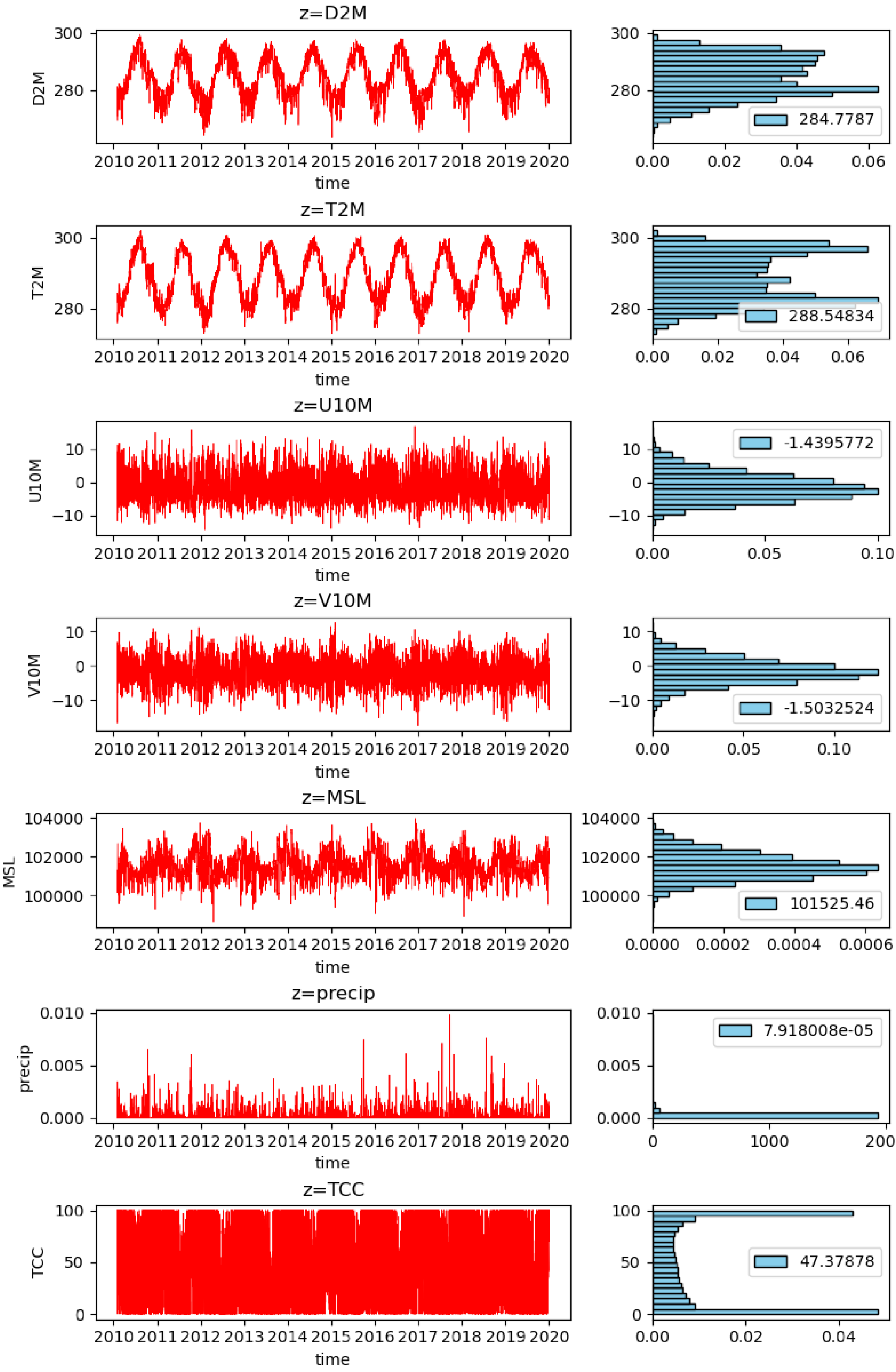

Figure 2.5: Temporal variations and mean value of atmospheric variables in the Black Sea, for the period from 2010 to 2019.

In order to support adaption measures and provide climate predictions, Data Marine Copernicus [1] provides accurate data on the past, present, and future climate in Europe and the rest of the world. The products selected and employed in this simulation for the input variables of physical tracers are denominated as:

- MEDSEA_MULTIYEAR_PHY_006_004
- BLKSEA_MULTIYEAR_PHY_007_004

for the point in the South Adriatic, and in the Black sea, respectively. These two products, contain the 3D daily mean fields: 3D potential temperature, salinity, which are required to establish the initial conditions. For the former dataset, the geographical extent covers the Mediterranean Sea from Latitude 30.18° to 45.98° and Longitude from -6° to 36.3° and it is defined on a regular grid at 1/24 degree (approx. 4km) and 141 vertical levels, as shown in Fig. 2.6a. The temporal resolution available is from 01.01.1987 to 30.06.2021.

For the second dataset, the geographical extent covers the Black Sea area from Latitude 40.86° to 46.8° and Longitudine from 27.32° to 41.96°. The model horizontal grid resolution is 1/27° in zonal resolution, 1/36° in meridional resolution (ca. 3 km) and has 31 unevenly spaced vertical levels as shown in Fig 2.6b.

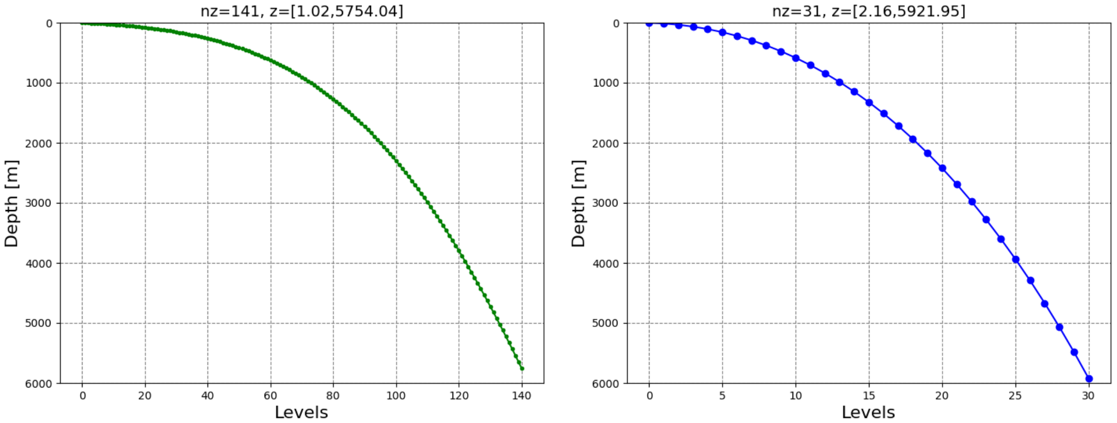

(a) Adriatic Sea (b) Black Sea

Figure 2.6: Vertical mesh used in the implementation sites with a sea depth of 702 m and 1342 m for the south Adriatic and Black Sea respectively. Levels near to the surface are more dense than those in the bottom.

The temporal resolution available is from 01.01.1993 to 31.12.2018 .

---

[1] see the Copernicus Climate Change Service `https://marine.copernicus.eu/`

In the reanalysis model, was utilized the two-band penetration scheme with the parameters ξ_0, ξ_1, and R, as specified in the namelist, The products are stored using the NetCDF format. A library that offers an implementation of the interface is called NetCDF (network Common Data Form), which is an interface for array-oriented data access.

In addition to the previously stated variables, the model output files also include numerous additional fields and attributes.

2.3.2 Chlorophyll source Dataset

The purpose of our study is to accurately derive the upper ocean thermal structures in two different penetration schemes. To achieve this, we make use of chlorophyll concentration. To determine the thermal structures of the ocean in the case of the RGB scheme, we use attenuation coefficients obtained from chlorophyll concentration (refer to Tab. 2.4 described in the next section).

On the other hand, in the two-band formulation, we define the water type based on chlorophyll concentration (Tab. 2.3). Additionally, a water optical categorization system is constructed. The datasets collected are provided from Copernicus Marine server and the products used are reanalysis, for the Mediterrean and Black sea biogeochemistry. They are referred as MEDSEA_MULTIYEAR_BGC_006_008 for the point in the Adriatic sea, and BLKSEA_REANALYSIS_BIO_007_005 for the station in the Black sea.

The Mediterranean Sea biogeochemical reanalysis at 1/24° of horizontal resolution (ca. 4 km) covers the period from Jan 1999 to 1 month to the present and is produced by means of the MedBFM3 model system.

The vertical grid is composed of 125 unevenly spaced levels and the geographical extent fills the Mediterrean sea area (5.54°W – 36.30°E; 30.18°N – 45.98°N). The data assimilation is made by satellite observations of chlorophyll.

This reanalysis provides 3D daily and monthly mean concentration of chlorophyll and the interim datasets are updated monthly. Black Sea Biogeochemistry Reanalysis has a 3 km horizontal resolution and the vertical grid is composed of 31 unevenly spaced vertical z-levels. The pruduct covers the Black sea area (27.37°E - 41.96°E; 40.86°N - 46.80°N). The temporal extent is since 1 Jan 1992 and timeseries extension is performed twice a year and the interim datasets are instead updated every month. For the daily dataset, the fields are daily means over a day (midnight to midnight, centred at noon).

The concentrations of chlorophyll throughout the simulation period in the Black Sea and the southern Adriatic are presented below (Fig 2.7, 2.8).

The average chlorophyll value has been calculated over the years, resulting in a value of 0.10 mg m^{-3} for the southern Adriatic and 0.40 mg m^{-3} for the Black Sea. These average chlorophyll values were necessary to deduce the attenuation length coefficients which will be discussed in the subsequent section.

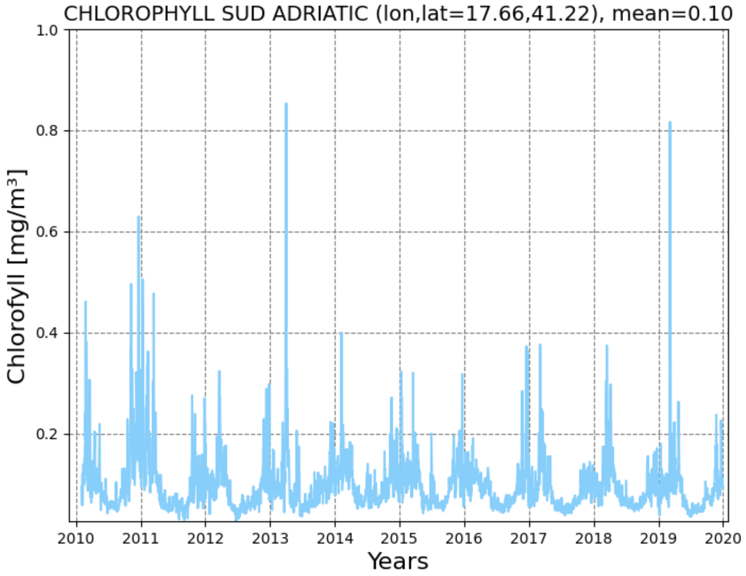

Figure 2.7: Clorophyll concentration and mean value of 0.10 mg m^{-3} in the point of South Adriatic from 2010 to 2019.

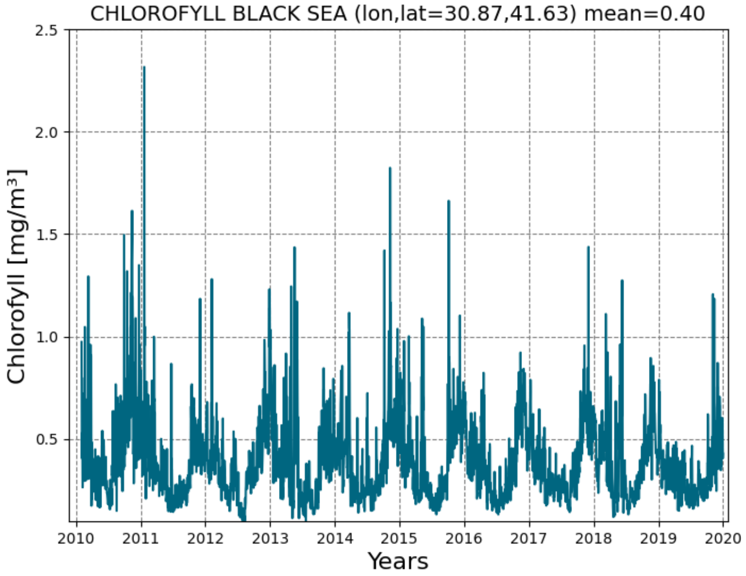

Figure 2.8: Clorophyll concentration and mean value of 0.4 mg m^{-3} in the point of Black Sea from 2010 to 2019.

2.4 Solar radiation penetration schemes

The purpose in this thesis is to investigate and study the impact of different absorption schemes of solar radiation on the vertical ocean thermal structures. Two different penetration schemes available in the NEMO code are used: the two-band penetration scheme (2band_scheme) and the scheme incorporating the presence of chlorophyll (rgb_scheme). The options for configuration are determined by the namtra qsr namelist variables. When the option for penetrative solar radiation is enabled (ln_flxqsr=true), solar radiation can penetrate into the upper tens of meters of the ocean. However, if this option is disabled (ln_flxqsr=false), all the heat flux is absorbed at the surface ocean level. Consequently, in the former case, an additional term is incorporated into the equation governing the time evolution of temperature (2.8), and the surface boundary condition is adjusted to consider only the non-penetrative component of the surface heat flux.

$$\frac{\partial T}{\partial t} = \ldots + \frac{1}{\rho_0 C_\mathrm{p}} \frac{\partial I\left(F_\mathrm{sol}, z\right)}{\partial z} \tag{2.10}$$

where I is the downward irradiance and Q_{sr} is the penetrative part of the surface heat flux (i.e. the shortwave radiation).

The shortwave radiation, encompasses energy distributed across a broad range of wavelengths (300 nm to 2800 nm). Within this range, the ocean strongly absorbs wavelengths longer than 700 nm (the near-infrared (NIR) band).

Because of the enormously large absorption coefficients of water molecules, this portion of solar radiation is quickly lost in the upper 2 m (Kara, Wallcraft, and Hurlburt [15]). The fraction of Q_{sr} that resides within these low penetrative wavelengths is denoted as R, (e.g. it is approximately 58% for the water type I, specified by the namelist parameter rn_abs). It is assumed to penetrate the ocean with a decreasing exponential profile, with an e-folding depth scale, ξ_0, of a few tens of centimeters (e.g. it is approximately 0.35 m for type water I, specified by the namelist parameter rn_si0).

For shorter wavelengths (400-700 nm), the ocean is more transparent, and solar energy propagates to larger depths where it contributes to local heating. The way this second part of the solar energy penetrates into the ocean depends on which formulation is chosen.

2.4.1 2-Band and RGB formulation

In the simple 2-waveband light penetration scheme (ln_qsr2bd=true), a chlorophyll-independent monochromatic formulation is chosen for the shorter wavelengths, leading to the following expression (Paulson and Simpson [24]):

$$I(z) = Q_{sr}\left[Re^{-z/\xi_0} + (1-R)e^{-z/\xi_1}\right] \tag{2.11}$$

where ξ_1 (specified by the namelist parameter rn_si0) represents the second extinction length scale related to the shorter wavelengths (400-700 nm). It is typically assigned a value of 23 m for Jerlov water types I, specifically referring to oligotrophic waters, as explained in section (1.4).

Based on the specific water type considered, different coefficients in the namelists need to be adjusted accordingly. In the presence of chlorophyll concentration data, the water type can be determined, and consequently, the corresponding parameters can be classified and modified as necessary, as shown in Tabs (2.2) and (2.3). The ocean's absorption of light relies on particle concentration and is selective across different wavelengths. Morel [22] demonstrated that an accurate representation of light penetration can be achieved using a detailed 61 waveband formulation. However, this model requires significant computational resources.

To address this limitation, Lengaigne et al. [19] developed a simplified version that divides visible light into three wavebands: blue (400-500 nm), green (500-600 nm), and red (600-700 nm).

The attenuation coefficient for each waveband, which depends on chlorophyll concentration, is approximated by fitting it to coefficients derived from Morel's comprehensive spectral model , as adjusted by Morel and Maritorena, while assuming a similar power-law relationship. This simplified formulation, known as RGB (Red-Green-Blue), closely replicates the light penetration profiles predicted by the full spectral model, while offering significantly improved computational efficiency.

On the other hand, the 2-bands formulation falls short of accurately reproducing the complete model.

Lastly, it should be noted that in areas with shallow ocean depths ($<$ 200 m), a certain amount of solar radiation can penetrate through and reach the ocean floor. In these scenarios, it is assumed that any remaining radiation is completely absorbed within the deepest accessible ocean layer. As previously indicated in the preceding section, based on the average chlorophyll values (Fig. 2.7, 2.8), the corresponding coefficients (ξ_0, ξ_1, R) were derived and subsequently incorporated into the respective namelist_ref configurations. This step was crucial in tailoring the simulations to accurately represent the distinctive characteristics of each water type, as outlined in the following tables (2.2 and 2.3).

Water types	I	IA	IB	II	III
ξ_0	0.35	0.6	1.0	1.5	1.4
ξ_1	23	20	17	14	7.9
R	0.58	0.62	0.67	0.77	0.78

Table 2.2: Paulson and Simpson [24] give an estimated relation between Jerlov water types (I to III) and attenuation length coefficients ξ_0, ξ_1.

Chlorophyll (mg m^{-3})	0-0.01	0.05	0.1	0.4	1.5-2.0
Jerlov water type	I	IA	IB	II	III

Table 2.3: Morel [22] gives a very approximate corrispondence between Jerlov water types (I to III) and chlorophyll concentration.

In our study, we specifically selected a type IB water classification to represent the southern Adriatic region, while a type II water classification was chosen to characterize the Black Sea. The corresponding coefficients associated with these water types were carefully determined and utilized in the respective simulations to ensure accurate representation. Below, the table (2.4) is provided, used by NEMO to calculate the attenuation coefficients related to the three spectral bands, associated with the wavelengths corresponding to the blue, green, and red colors.

Chlorophyll	Blue	Green	Red
0.010	0.01618	0.07464	0.37807
0.011	0.01654	0.07480	0.37823
0.013	0.01693	0.07499	0.37840
0.014	0.01736	0.07518	0.37859
0.016	0.01782	0.07539	0.37879
0.018	0.01831	0.07562	0.37900
0.020	0.01885	0.07586	0.37923
0.022	0.01943	0.07613	0.37948
0.025	0.02005	0.07641	0.37976
0.028	0.02073	0.07672	0.38005
0.032	0.02146	0.07705	0.38036
0.035	0.02224	0.07741	0.38070
0.040	0.02310	0.07780	0.38107
0.045	0.02402	0.07821	0.38146
0.050	0.02501	0.07866	0.38189
0.056	0.02608	0.07914	0.38235
0.063	0.02724	0.07967	0.38285
0.071	0.02849	0.08023	0.38338
0.079	0.02984	0.08083	0.38396
0.089	0.03131	0.08149	0.38458
0.100	0.03288	0.08219	0.38526
0.112	0.03459	0.08295	0.38598
0.126	0.03643	0.08377	0.38676
0.141	0.03842	0.08466	0.38761
0.158	0.04057	0.08561	0.38852
0.178	0.04289	0.08664	0.38950
0.200	0.04540	0.08775	0.39056
0.224	0.04811	0.08894	0.39171
0.251	0.05103	0.09023	0.39294
0.282	0.05420	0.09162	0.39428
0.316	0.05761	0.09312	0.39572
0.355	0.06130	0.09474	0.39727
0.398	0.06529	0.09649	0.39894
0.447	0.06959	0.09837	0.40075
0.501	0.07424	0.10040	0.40270
0.562	0.07927	0.10259	0.40480
0.631	0.08470	0.10495	0.40707
0.708	0.09056	0.10749	0.40952
0.794	0.09690	0.11024	0.41216
0.891	0.10374	0.11320	0.41502
1.000	0.11114	0.11639	0.41809
1.122	0.11912	0.11984	0.42142
1.259	0.12775	0.12356	0.42500
1.413	0.13707	0.12757	0.42887
1.585	0.14715	0.13189	0.43304
1.778	0.15803	0.13655	0.43754
1.995	0.16978	0.14158	0.44240
2.239	0.18248	0.14701	0.44765
2.512	0.19620	0.15286	0.45331
2.818	0.21102	0.15918	0.45942
3.162	0.22703	0.16599	0.46601
3.548	0.24433	0.17334	0.47313
3.981	0.26301	0.18126	0.48080
4.467	0.28320	0.18981	0.48909
5.012	0.30502	0.19903	0.49803
5.623	0.32858	0.20898	0.50768
6.310	0.35404	0.21971	0.51810
7.079	0.38154	0.23129	0.52934
7.943	0.41125	0.24378	0.54147
8.912	0.44336	0.25725	0.55457
10.000	0.47804	0.27178	0.56870

Table 2.4: The table presents the attenuation coefficients used by NEMO in the RGB (red-green-blue) formulation in relation to the chlorophyll concentration.

On the next page, we display the graph representing the attenuation coefficients of the three spectral bands as a function of chlorophyll concentration.

Based on the chlorophyll concentration present in the water, solar radiation penetrates in different ways. In the RGB formulation, the fraction of visible light of shortwave radiation Q_{sr} is split into three spectral bands (blue (B): 415nm-490nm, green (G): 500nm-595nm, and red (R): 615nm-760nm). Each spectral band, as shown in Fig 1.4, has a corresponding attenuation coefficient.

What emerges from the graph is that the curve related to the red band, having a longer wavelength, shows a higher attenuation coefficient compared to the other two. This is because with a lower frequency, solar radiation only penetrates the first tens of meters. It is noticeable that for high chlorophyll concentration values, the attenuation coefficient is higher. This is because as the amount of chlorophyll becomes significant, the penetration of solar radiation along the water column becomes more challenging.

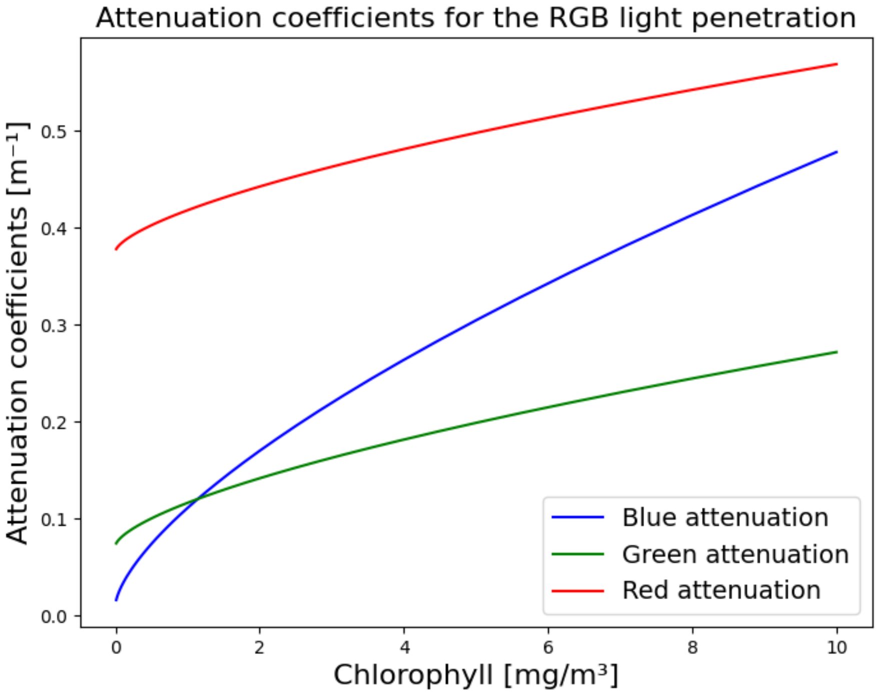

Figure 2.9: Variations of attenuation coefficients as a function of chlorophyll concentration.

CHAPTER 3

Solar radiation field in natural waters: sensitivity experiments and analysis

3.1 Comparison of different penetration schemes

Through the following sections, our aim is to give the reader an overview of the vertical profile of temperature obtained with the NEMO1D simulations in the two selected locations. We will analyze the CMEMS-reanalysis model data to gain insights into these profiles. In this context, we will investigate the effect of various penetration schemes on the water column and we will compare them with a more realistic CMEMS reanalisys products. The employed vertical mixing scheme parametrization and surface boundary condition fields we used in NEMO1D are the same as those used in CMEMS reanalisys models. This analysis will help to define the importance of different penetration schemes within the scope of our study.

3.1.1 Temperature profiles

The figures presented in this section show the vertical profiles of temperature at two specific locations: the South Adriatic site and the the Black Sea site. Firstly, temperature profiles were showed in the Upper Ocean (100m) where the shortwave radiation can affects the ocean heat content and so the temperature structure.

The daily mean temperature profiles were shown at three different days during the year 2016. We chose to focus on a single year to better appreciate the seasonal variability. Specifically, we selected one day in spring, one in summer, and one in late autumn in order to appreciate the variation of the vertical upper ocean temperature structures across the seasons. The selected days corresponds, respectively, to April 5, July 11, and November 20, 2016. These dates allow us to observe the changes and trends in temperature profiles over the course of the year. First, we display the temperature profiles related to the South Adriatic site, and then we will show those of the Black Sea site.

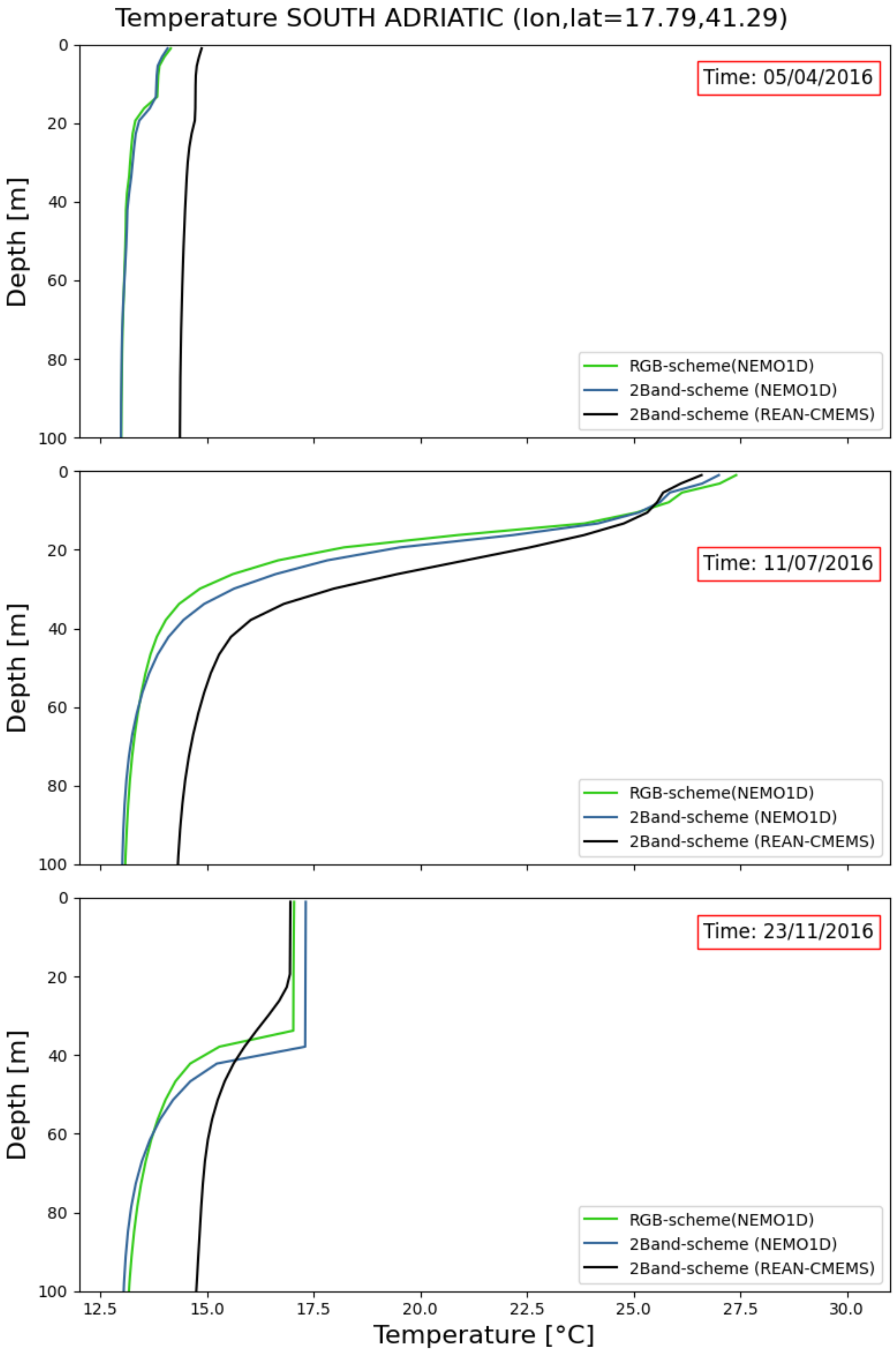

Figure 3.1: Daily mean temperature profiles in the South Adriatic site in three different days of the 2016, April 5 (top panel), July 11 (central panel), November 20 (bottom panel). Each panel shows the comparison between NEMO1D-RGB, NEMO1D-2Band and CMEMS-Reanalysis model.

The daily temperature profile on April 5, corresponding to the two penetration schemes, shows a slight thermocline at around 10 meters. In contrast, in the temperature profile of the reanalysis data, this difference is less pronounced. The surface temperature in all three profiles is approximately 15 °C. As we descend in depth, the reanalysis profile remains relatively constant, similar to the other two profiles obtained from the RGB and 2-band formulations. At the surface, the temperature in the RGB scheme is a little bit higher compared to the other scheme. The two profiles follow the same trend and overlap around 30 meters. From 20 meters onwards, there is a difference of approximately 2 °C between the temperature in the reanalysis data and the two penetration schemes.

During the summer period, first of all, we observe a pronounced thermocline ranging from 10 to 30 meters. Again, the surface temperature in the RGB profile is higher compared to the other two schemes, and it's around 27.5 °C. The three profiles intersect around 15 meters and then diverge for the rest of the vertical column.

We notice that the temperatures in the RGB and 2-band schemes assume the same temperature value as the reanalysis profile, but at shallower depths. As we descend further, the temperature profiles from the two penetration schemes deviate by a few degrees from the reanalysis profile. Around 50 meters, these two profiles overlap and then decrease steadily for the rest of the depth, just like the temperature profile from the reanalysis data. In the last graph, corresponding to the winter profile, we immediately notice that the thermocline almost disappears. In this case, the higher surface temperature is associated with the 2-band scheme. The surface temperatures in all three profiles are approximately the same, around 17 °C. From 20 meters onwards, we can observe two different behaviors.

The temperature trend in the reanalysis model slightly decreases until 60 meters, where it reaches a temperature of 15 °C, which remains constant for the rest of the depth. As for the profiles of the other two schemes, we can see that the temperature remains constant until 40 meters, maintaining a value of approximately 17 °C.

From this point, the temperature decreases more noticeably, reaching 13 °C at around 50 meters, where the two profiles overlap and maintain the same trend for the rest of the water column.

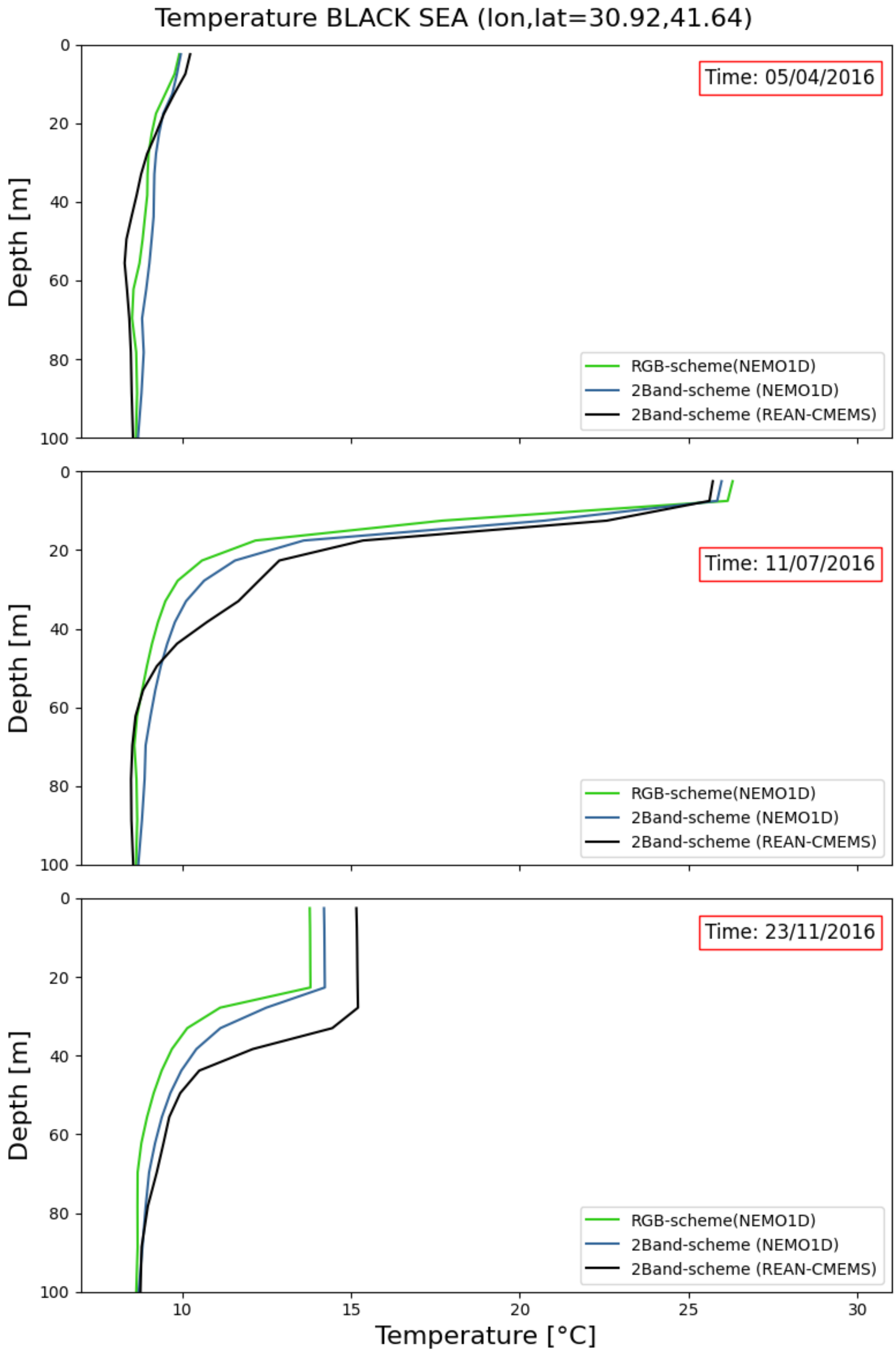

Figure 3.2: Daily mean temperature profiles for the first timestep in the Black Sea site in three different days of the 2016, April 5 (top panel), July 11 (central panel), November 20 (bottom panel). Each panel shows the comparison between NEMO1D-RGB, NEMO1D-2Band and CMEMS-Rean model.

Starting with the first timestep, the temperature obtained using the RGB scheme is lower compared to the other two schemes for the first 25 meters.

Subsequently, all temperatures gently decrease, and the temperature curve relative to the reanalysis data slightly diverges from the other two, assuming a lower value. Meanwhile, the temperature associated with the 2-Band scheme takes on a higher value for the remaining depths. From 80 meters onwards, the three profiles follow the same trend, and the temperature constantly decrease.

Reaching the 100 meters, the temperature profiles of the two schemes overlap and then maintain the same trend throughout the rest of the depths.

In summer, we can highlight a well pronounced thermocline, which occurs at depths of approximately 10 to 20 meters. At the surface, the temperatures in all three schemes reach values greater than 25 °C. The three profiles intersect around 10 meters, and from this point , the temperature profile of the reanalysis model deviates from the other two profiles. The temperature decreases significantly from 15 meters onwards, starting from a value of 24 °C, reaching, at 40 meters, 16 °C and 14 °C for the reanalysis and the others two formulations, respectively.

The profiles follow the same trend, with the result that the curves corresponding to the two penetration schemes deviate even further from the reanalysis profile, assuming the same temperature value but at lower depths. From this point onwards, all temperature profiles decrease fairly consistently. Around 60 meters, the trends of the two schemes overlap for the remaining depths. In winter, the thermocline almost disappears as the temperature remains relatively constant in the first few tens of meters.

In this case, the surface temperature in the reanalysis model has a higher value compared to the other two schemes, at 15 °C. The temperature profiles of the two schemes remain constant until approximately 20 meters, while the reanalysis profile exhibits the same behavior until 30 meters. From 30 to 60 meters, the reanalysis profile deviates from the other two schemes, showing the same temperatures but at greater depths.

In this range, the temperature decreases almost exponentially for all three profiles. They converge again around 70 meters, where they maintain a constant trend for the rest of the water column.

3.2 Annual variability

In this section the daily mean temperature profiles for our points of interest covering the duration of the entire simulation (from 2010 to 2019 inclusive) are presented. The profiles corresponding to the two different penetration schemes will be shown, along with their differences with the CMEMS reanalysis model.
The temperature differences are indicated in red and blue, respectively, for positive and negative deviations in values.

3.2.1 South Adriatic site

Figure 3.3 shows the temperature distribution along the water column in the first 100 meters, corresponding to the CMEMS reanalysis model.
In this graph, contour lines have been added to highlight the temperatures marking 14 °C, aiming to underline the differences with other values. Subsequently, Figures 3.4a and 3.4b display the annual temperature profiles obtained using the RGB and 2-Band formulations, respectively. Here, two contour lines have been added to mark two different temperature ranges, specifically 14 °C and 15 °C, in order to highlight the variations more clearly. The differences between our experiments and CMEMS reanalysis model are shown in the panels on the right for the two-band (3.4c) and RGB (3.4d) penetration schemes.

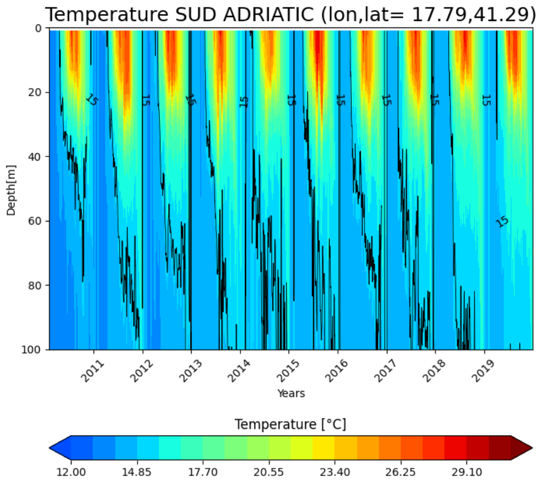

Figure 3.3: Daily mean temperature profile in the South Adriatic site from the CMEMS reanalysis model for the period 2010-2019.

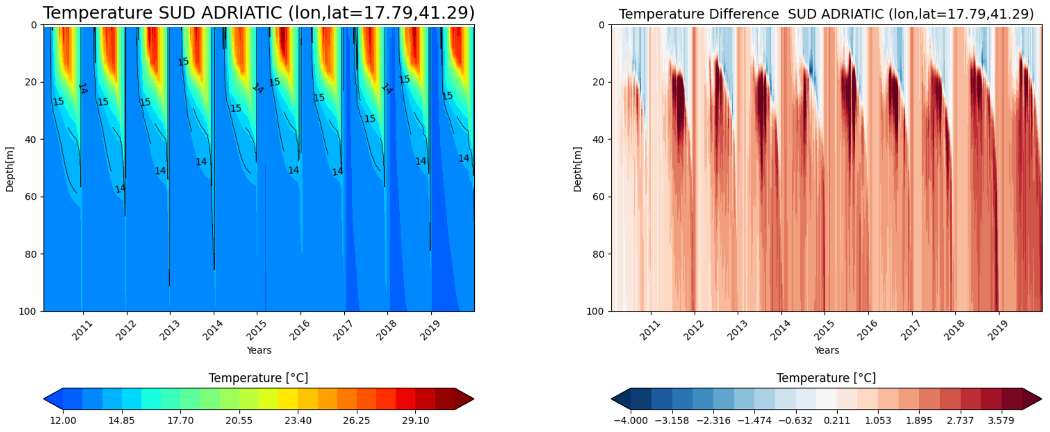

(a) NEMO1D-RGB formulation.

(c) (CMEMS-RGB) differences.

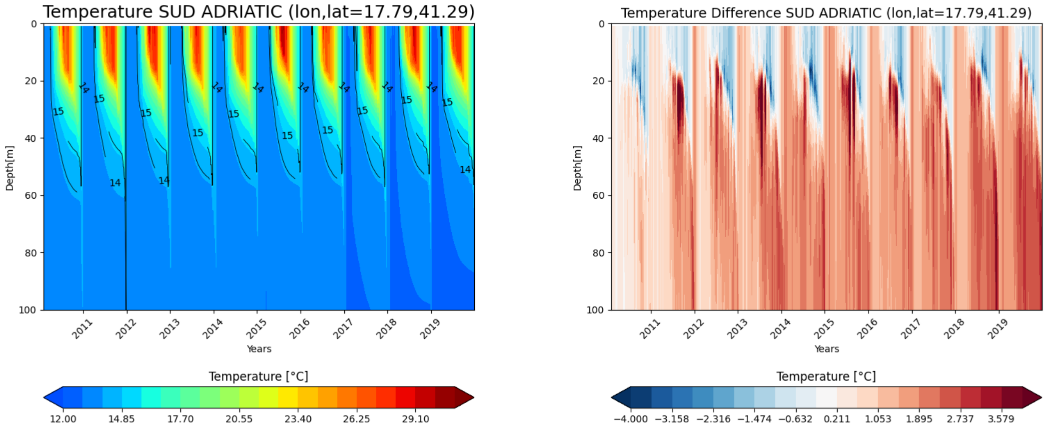

(b) NEMO1D-2-Band formulation.

(d) (CMEMS-2Band) differences.

Figure 3.4

In Fig. 3.4 are shown the daily mean vertical temperature profile in the South Adriatic site for the entire simulation period (2010 to 2019): (a) NEMO1D-RGB formulation, (b) NEMO1D-2Band formulation, (c,d) the difference between NEMO1D and CMEMS models.

The main differences between Figures 3.4a and 3.4b are related to the different penetration schemes used. In the first one, (3.4a), we can see how the temperature reaches 15°C and 14°C at depths of approximately 30 and 60 meters, respectively. We observe a layer with a lower temperature immediately following the layer associated with a temperature of 15°C. On the other hand, in the two-band formulation, (Figure 3.4b), the opposite behavior is highlighted. At 30 meters, we can observe a layer with a temperature of 14°C, followed immediately below by another layer with a value of 15°C. In both profiles, from 60 meters onwards, the temperature decreases steadily with depth. Regarding the temperature differences (ranging from -4°C to 4°C) in Figures 3.4c and 3.4d, we observe near-zero or negative variations in the first 20 meters. The maximum temperature difference recorded, approximately 4°C, occurs during the summer period. This discrepancy is observed from 20 to 40 meters and persists throughout the simulation. These differences decrease with depth, reaching a value of approximately 2 °C for the rest of the water column.

3.2.2 Black Sea site

Regarding the Black Sea, more pronounced differences can be observed between the two penetration schemes. Similarly, Figure 3.7 displays the annual temperature profile at a specific point in the Black Sea within the first 100 meters, obtained from the input reanalysis model.

In this graph, contour lines have been added to highlight the temperatures marking 8 °C, with the aim to emphasize the differences with other values. Figures 3.6a and 3.6b show the temperature profiles corresponding to the RGB and two-band formulations, respectively.

In this case, two contour lines have been included to delineate two distinct temperature ranges, specifically 8 °C and 9 °C, with the purpose of providing a clearer representation of the variations. Finally, Figures 3.6c and 3.6d highlight the most prominent differences among the various temperature profiles.

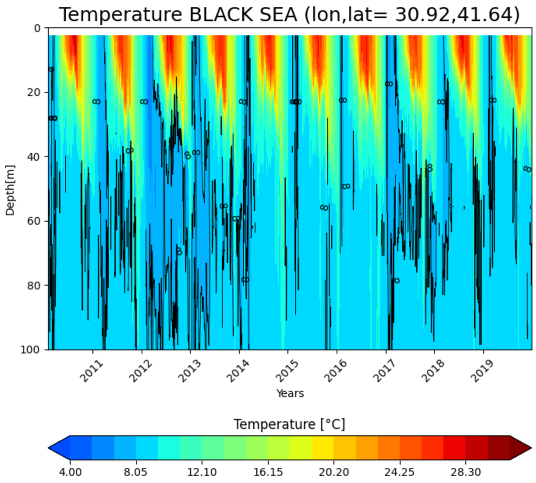

Figure 3.5: Daily mean temperature profile in the Black Sea site from the CMEMS reanalysis model for the period 2010-2019.

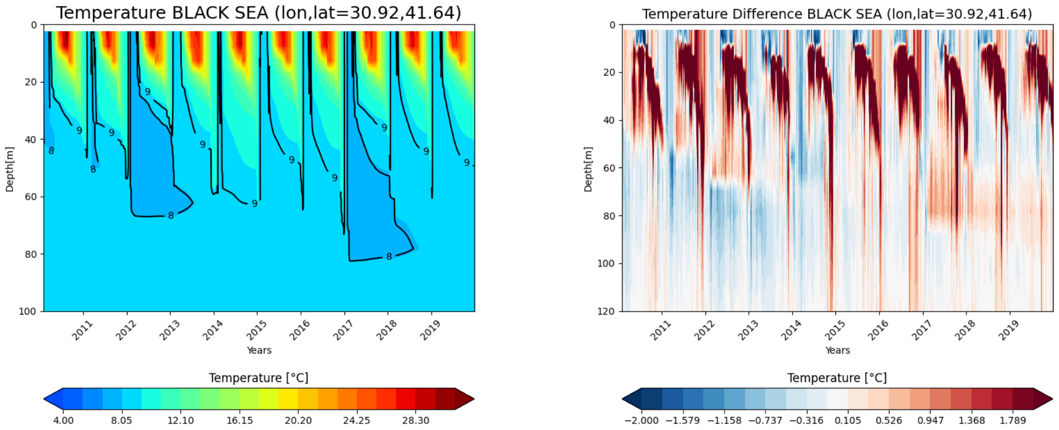

(a) NEMO1D-RGB formulation.

(c) (CMEMS-RGB) differences.

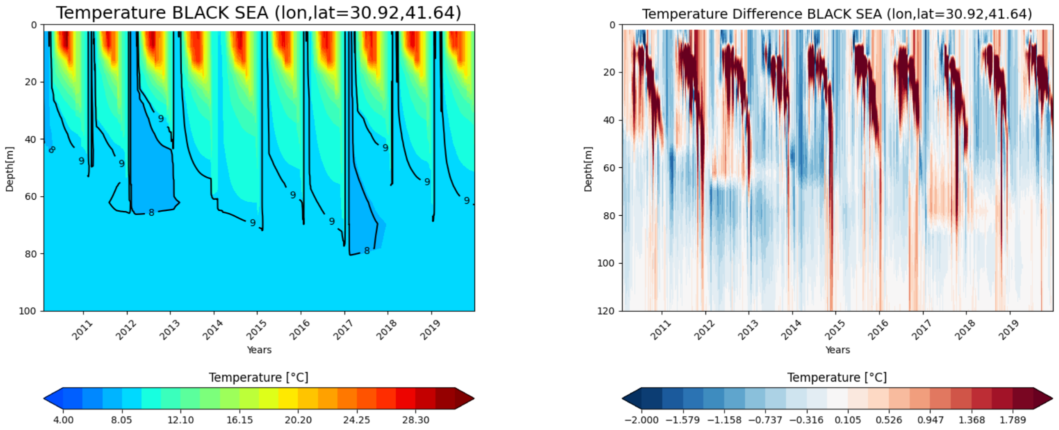

(b) NEMO1D-2-Band formulation.

(d) (CMEMS-2Band) differences.

Figure 3.6

In Fig. 3.6 are shown the daily mean vertical temperature profile in the Black Sea site for the entire simulation period (2010 to 2019): (a) NEMO1D-RGB formulation, (b) NEMO1D-2Band formulation, (c,d) the difference between NEMO1D and CMEMS models.

In both figures (Figure 3.6a and Figure 3.6b), layers corresponding to two different temperatures, 8 °C and 9 °C, are highlighted. Specifically, two distinct areas are noticeable, representing the years 2012/2013 and 2017/2018, where the temperature reaches 8 °C at depths of 60 and 80 meters, respectively.
In the temperature profile of the RGB scheme (Figure 3.6a), these temperature areas appear more pronounced compared to the two-band formulation. In Figure (3.6a), the regions measuring 8 °C seem to persist over a longer period of time compared to the temperature profile observed in the two-band formulation (Figure 3.6b), where they remain more confined to the specific area of interest.
The temperature differences (that range from -2°C to 2°C) in Figures (3.6c) and (3.6d), positive temperature variations are observed in the first 40 meters during the summer period. The most significant differences, measuring 2°C, occur throughout the slope associated with the thermocline. As depth increases, these variations become less pronounced. In fact, it can be noted that from approximately 80 meters onwards, the temperature difference approaches zero.

3.3 Root Mean Square Error

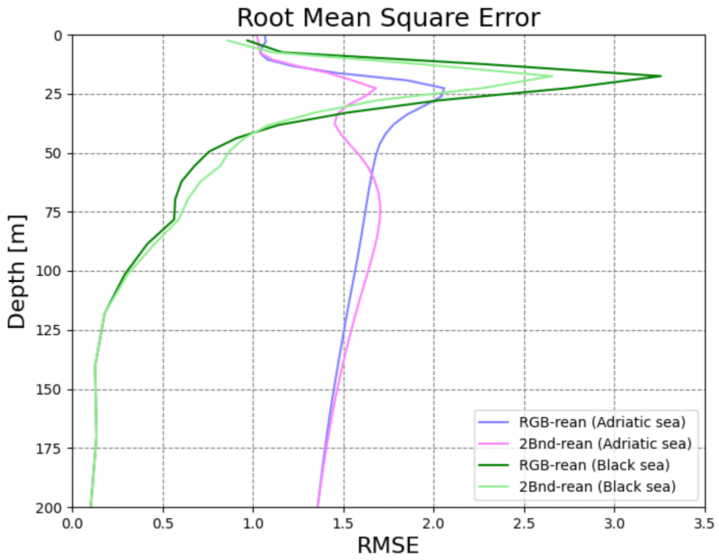

Figure 3.7: Root Mean Square Error for the different penetration schemes.

In order to test and quantify the accuracy of our simulations, we evaluate the root mean square error (RMSE) between the quantities simulated by each NEMO1D-model ψ_m and the CMEMS reanalisy quantities ψ_o, defined by:

$$RMSE = \sqrt{\frac{1}{N}\sum_{i}^{N}(\psi_m - \psi_o)^2} \tag{3.1}$$

Regarding the temperature profiles for the RGB scheme, we observed a higher discrepancy compared to the reanalysis model. The representation obtained with the two-band formulation exhibited a better fit to the reanalysis model, showing a lower RMSE. For both models associated with the two penetration schemes, we noticed that the RMSE values decrease with increasing depth. It is worth noting that for the Black Sea, the RMSE value approaches zero around a depth of 200 meters, whereas for the South Adriatic, it measures approximately 1.3.

Lastly, the RMSE can serve as an evaluation tool for optimizing model parameters. One approach could involve testing different parameter sets and selecting those that yield the lowest RMSE, indicating a better fit to the reference data.

CHAPTER 4

Results and conclusions

The optical properties of water were examined by conducting simulations using NEMO1D model, which was driven by monthly averaged chlorophyll observations. By examining the temperature profiles and the variations induced by different penetration schemes, we can assess how the model responds to these variations.
Assuming the reanalysis model as a reference, we observe that during the spring/winter period, the NEMO1D model underestimates the temperature in the mixed layer. Conversely, during the summer period, the temperature profile associated with the RGB model slightly overestimates the input reanalysis model.
The 1D model, focusing exclusively on the vertical dimension, neglects many processes, including the spatial variability of ocean circulation and processes occurring along latitudes and longitudes, hence the horizontal interactions.
Additionally, being a one-dimensional model, the NEMO1D model does not account for the complex feedback between the ocean and the atmosphere.
The reason for this temperature discrepancy may be also attributed to the inclusion of chlorophyll in our model. Its presence is likely to have influenced the vertical temperature profile.
Chlorophyll, being located in the surface layer of the water column, reflects and absorbs a significant amount of solar radiation, preventing it from penetrating into the lower layers. The ability to classify different water types based on average chlorophyll concentrations further enhances our understanding of these complex systems. However, wind events that could have influenced the mixing of water columns might

not be captured in monthly measurements of salinity and temperature.

The observed inter-annual variability in temperature profiles is determined by annual changes in chlorophyll input and circulation dynamics (including wind-driven circulation).

This thesis contributes to the field of underwater radiation and its impact on water properties. The results provide insights for future studies and modeling efforts aimed at improving our understanding of solar radiation penetration and its effects on water environments.

Overall, these findings highlight the influence of different formulations and model assumptions on the vertical temperature profiles and emphasize the importance of considering factors such as chlorophyll distribution and horizontal advection in accurately simulating temperature variations in the water column.

Future research can consider conducting one-dimensional studies using high-resolution forcing data, particularly to comprehensively analyze the nutrient dynamics and the resulting changes in the primary production cycle.

Future developments can include comparisons with pure observational data and the extension of this sensitivity analysis to 3D models, as they provide higher accuracy.

Bibliography

[1] John R Apel. *Principles of ocean physics.* Academic Press, 1987.

[2] A Artegiani et al. “The Adriatic Sea general circulation. Part I: Air–sea interactions and water mass structure”. In: *Journal of physical oceanography* 27.8 (1997), pp. 1492–1514.

[3] GHASSEM ASRAR. “Estimation of plant-canopy attributes from spectral reflectance measurements”. In: *Theory and application of optical remote sensing* (1989), pp. 252–296.

[4] Edward T Baker and J William Lavelle. “The effect of particle size on the light attenuation coefficient of natural suspensions”. In: *Journal of Geophysical Research: Oceans* 89.C5 (1984), pp. 8197–8203.

[5] DJ Bernie et al. “Impact of resolving the diurnal cycle in an ocean–atmosphere GCM. Part 1: A diurnally forced OGCM”. In: *Climate Dynamics* 29 (2007), pp. 575–590.

[6] Giovanni Coppini et al. “The Mediterranean forecasting system. Copernicus Monitoring Environment Marine Service (CMEMS)”. In: (2021).

[7] Benoit Cushman-Roisin et al. *Physical oceanography of the Adriatic Sea: past, present and future.* Springer Science & Business Media, 2013.

[8] Glenn R Flierl and Cabell S Davis. “Biological effects of Gulf Stream meandering”. In: *Journal of Marine Research* 51.3 (1993), pp. 529–560.

[9] RW Gould and RA Arnone. “Optical water mass classification for ocean color imagery”. In: *Second International Conference, Current Problems in Optics Of Natural Waters. St. Petersburg, Russia.* 2003.

[10] Madec Gurvan et al. *NEMO ocean engine.* Version v3.6-patch. Fix broken cross-references, still revision 8625 from SVN repository. Oct. 2017. DOI: `10.5281/zenodo.3248739`. URL: `https://doi.org/10.5281/zenodo.3248739`.

[11] Hans Hersbach et al. “The ERA5 global reanalysis”. In: *Quarterly Journal of the Royal Meteorological Society* 146.730 (2020), pp. 1999–2049.

[12] Nils G Jerlov. “Optical classification of ocean water”. In: *Physical aspects of light in the sea.* University of Hawaii Press, 2021, pp. 45–50.

[13] Nils Gunnar Jerlov. *Marine optics.* Elsevier, 1976.

[14] Nils Gunnar Jerlov. “Optical studies of ocean water”. In: *Rept. Swedish Deep-Sea Exped.* 3 (1951), pp. 1–59.

[15] A Birol Kara, Alan J Wallcraft, and Harley E Hurlburt. “A new solar radiation penetration scheme for use in ocean mixed layer studies: An application to the Black Sea using a fine-resolution hybrid coordinate ocean model (HYCOM)”. In: *Journal of physical oceanography* 35.1 (2005), pp. 13–32.

[16] J.T.O. Kirk. “Dependence of relationship between inherent and apparent optical properties of water on solar altitude”. In: *Limnology and Oceanography* 29.2 (1984), pp. 350–356.

[17] J.T.O. Kirk. “Effects of suspensoids (turbidity) on penetration of solar radiation in aquatic ecosystems”. In: *Hydrobiologia* 125 (1985), pp. 195–208.

[18] Konstantin Korotenko. “Effects of mesoscale eddies on behavior of an oil spill resulting from an accidental deepwater blowout in the Black Sea: An assessment of the environmental impacts”. In: *PeerJ Computer Science* 6 (Aug. 2018), e5448. DOI: `10.7717/peerj.5448`.

[19] Matthieu Lengaigne et al. “Influence of the oceanic biology on the tropical Pacific climate in a coupled general circulation model”. In: *Climate Dynamics* 28 (2007), pp. 503–516.

[20] K.J. McCree. “A solarimeter for measuring photosynthetically active radiation”. In: *Agricultural Meteorology* 3.5-6 (1966), pp. 353–366.

[21] Fedor Mesinger and Akio Arakawa. “Numerical methods used in atmospheric models”. In: (1976).

[22] André Morel. “Optical modeling of the upper ocean in relation to its biogenous matter content (case I waters)”. In: *Journal of geophysical research: oceans* 93.C9 (1988), pp. 10749–10768.

[23] M Orlic, M Gacic, and PE Laviolette. “The currents and circulation of the Adriatic Sea”. In: *Oceanologica acta* 15.2 (1992), pp. 109–124.

[24] Clayton A Paulson and James J Simpson. “Irradiance measurements in the upper ocean”. In: *Journal of Physical Oceanography* 7.6 (1977), pp. 952–956.

[25] Helmut Piazena and Donat-P Häder. “Penetration of solar UV and PAR into different waters of the Baltic Sea and remote sensing of phytoplankton”. In: *The effects of ozone depletion on aquatic ecosystems* (1997), pp. 45–96.

[26] Robin M Pope and Edward S Fry. “Absorption spectrum (380–700 nm) of pure water. II. Integrating cavity measurements”. In: *Applied optics* 36.33 (1997), pp. 8710–8723.

[27] Rudolph W Preisendorfer. *Hydrologic optics*. US Department of Commerce, National Oceanic and Atmospheric Administration . . ., 1976.

[28] Guillaume Reffray, Romain Bourdalle-Badie, and Christophe Calone. “Modelling turbulent vertical mixing sensitivity using a 1-D version of NEMO”. In: *Geoscientific Model Development* 8.1 (2015), pp. 69–86.

[29] Raymond C Smith and Karen S Baker. “Optical properties of the clearest natural waters (200–800 nm)”. In: *Applied optics* 20.2 (1981), pp. 177–184.

[30] Michael G Solonenko and Curtis D Mobley. “Inherent optical properties of Jerlov water types”. In: *Applied optics* 54.17 (2015), pp. 5392–5401.

[31] Aurore Voldoire et al. “The CNRM-CM5. 1 global climate model: description and basic evaluation”. In: *Climate dynamics* 40 (2013), pp. 2091–2121.

[32] Craig A Williamson and Richard C Hollins. “Measured IOPs of Jerlov water types”. In: *Applied Optics* 61.33 (2022), pp. 9951–9961.